A Strategy to Build High-performance Thick Electrodes for Lithium-ion Batteries with Enhanced Compressive Modulus and Regulated Tortuosity in Phase-inversion Processing

Yifan Zhang[1], Yaohong Xiao[2], Lei Chen[2], Shan Hu[1, *]

[1] Department of Mechanical Engineering, Iowa State University, 2529 Union Drive, Ames, IA 50010, USA

[2] Department of Mechanical Engineering, University of Michigan-Dearborn, 4901 Evergreen Road, Dearborn, MI 48128, USA

* Corresponding author: shanhu@iastate.edu

Key words: Thick electrodes, lithium-ion batteries, phase inversion, tortuosity, compressive modulus

Abstract

Building low-tortuosity thick electrodes, which is a practical strategy to boost energy density of lithium-ion batteries (LIBs) by improving ion transport, has been investigated widely. As one of the effective and low-cost methods to form vertically aligned porous architectures, phase-inversion has been explored to enhance the performance of electrodes. Despite the achievement of electrodes with high mass loading and brilliant electrochemical performance via phase-inversion processing, poor mechanical properties of the electrode impede its application in large-scale devices, such as electric vehicles (EVs). Herein, we develop a method to upgrade the compressive strength of $LiFePO_4$ (LFP) electrodes by tuning the components in non-solvent used in the non-solvent induced phase-inversion based electrode fabrication. With the introduction of ethanol in the non-solvent bath, compressive modulus of low-tortuosity LFP electrode with loading of 40 mg/cm^2 reaches up to 18.1 MPa, around four times higher than the electrodes processed in only water with the same mass loading. Additionally, low-tortuosity LFP electrode produced with mixture of water and ethanol exhibits superior rate capability (73.3 mAh/g at 2 C) and cycling stability (89.3% capacity retention after 100 cycles at 0.5 C). Furthermore, electrodes with different mass loadings (20 and 30 mg/cm^2) but similar tortuosity was obtained by adjusting the duration of immersion during the phase-inversion processing with the same non-solvent bath. This report provides a novel approach to elevate mechanical robustness of high-performance thick electrodes produced through phase-inversion as well as more precise control of the microstructures.

1 Introduction

Lithium-ion batteries (LIBs) have been widely adopted in various fields ranging from consumer electronics to electric vehicles (EVs). To meet the growing demand of energy storage, high-performance LIBs have been continuously developed through new electrode materials and battery chemistries[1–4]. One of the practical strategies to improve energy density of LIBs is to increase the thickness of their electrodes, which reduces the ratio of electrochemically inactive materials (e.g., current collectors, separators, additives, and packaging materials)[5–7]. In conventional design of electrodes, randomly packed particles of active materials induce high tortuosity for the pathway of lithium-ion diffusion. The relation between porosity, tortuosity, and effective diffusivity is

expressed as: $D_{eff} = \varepsilon D_0/\tau$, in which D_{eff} and D_0 represent effective and intrinsic diffusivity, respectively, and ε and τ stand for porosity and tortuosity, respectively. This indicates that a higher tortuosity decreases effective diffusivity for a given porosity in the electrode, which can result in drastic reduction in available capacity of active materials and therefore reduced energy density as charging/discharging rate increases[8–10]. This deterioration of performance is especially severe in thick electrodes with high tortuosity[11–13].

In recent years, various methods have been developed to engineer the architecture of electrodes to facilitate the diffusion of lithium-ions in battery electrodes, such as magnetic templating[14,15], phase-inversion[16–25], channel-drilling[26,27], freeze-casting[28–36] and acoustic-field modulation[37], nanoarray engineering[38], stamping process[39], screen printing[40]. Among these novel manufacturing methods, phase-inversion is an outstanding approach in terms of efficiency and scalability for generating low-tortuosity structures[41]. For the commonly adopted procedures of battery electrode fabrication, active materials and conductive additives are dispersed in polymer binder solution to form the electrode slurry. The phase-inversion method involves three components including polymer, solvent, and non-solvent, which is non-compatible or weakly compatible with the polymer. After the slurry of battery electrode is coated on the substrate, the coating layer (with polymer binder solution) and the substrate together will be immersed in the non-solvent bath. The concentration gradient continuously drives the solvent out and the non-solvent into the polymer solution, resulting in phase separation that produces a polymer network with various microstructures inside the non-solvent[42,43]. Furthermore, due to the excellent binding between the polymer binder and the particles of active materials and conductive additives, the phase inversion of the polymer will also modulate the spatial distribution of these particles and therefore the structures of the resulting electrode. When phase inversion conditions are controlled, low-tortuosity structures such as vertically aligned channels can be formed in the battery electrodes.

Despite the advantage that phase-inversion method has demonstrated in terms of improving the electrochemical performance of battery electrodes, the electrodes' low resistance to deformation (or low modulus), similarly to electrodes with high porosity, has been one of the overdue issues that needs to be addressed[44–46]. Easy deformability because of low modulus posts great challenge to maintain thick electrodes' mechanical robustness, which is critical for the safety and cyclic stability of batteries. Compressive modulus is a critical mechanical property for thick electrodes because when electrodes are assembled into cells, they are always subjected to "compressive stack pressure" to ensure good contact between different components. In addition, during charging/discharging, electrode will undergo volume change which can induce additional compressive stress on the electrode because they are constrained inside a battery pack [47]. In this work, we report a strategy to enhance the mechanical robustness of $LiFePO_4$ (LFP) electrodes fabricated by phase-inversion method through tuning the composition of non-solvent bath. Specifically, instead of using water as non-solvent in existing work[20,21,23], ethanol of different volume ratios was mixed with water to form the non-solvent. With a higher ratio of ethanol in the non-solvent, higher compressive modulus of low-tortuosity LFP electrodes was achieved. On the other hand, with the same areal mass loading of active materials, electrode processed by higher ethanol ratio showed better rate performance and cycling stability. For instance, LFP electrodes with areal mass loading of ~ 40 mg/cm^2 immersed in non-solvent bath with 3:1 volumetric ratio

of deionized water (DIW) to ethanol delivered specific capacity of 73.3 mAh/g at rate of 2 C and the capacity retention of 89.3% after 100 cycles at 0.5 C, compared to 37.2 mAh/g and retention of 58.2% by LFP electrodes processed by only DIW at the same rate. Moreover, with the same non-solvent, immersion time can be adjusted for electrodes with varied thickness to achieve similar structural tortuosity. This investigation provides a facile phase-inversion-based method to not only promote the electrochemical performance but also improve the compressive modulus of electrode.

2 Experiment

2.1 Preparation of low-tortuosity LFP electrodes

For the preparation of slurry, LFP powder (D50 = 1.5 μm, MSE supplies) and acetylene black (Alfa Aesar, 100% compressed) were dispersed in N-methyl-2-pyrrolidone (NMP) (Sigma Aldrich) solvent containing polyvinylidene fluoride (PVDF) (M_w ~ 180,000 g/mol, Sigma Aldrich) with ratio of LFP, PVDF and acetylene black as 65:20:15. Mechanical stirring was applied overnight for uniform dispersion of solid materials in the slurry. The prepared slurry was cast on a glass slide to form a wet film. The thickness of the wet film is controlled by doctor blade coater to achieve the target areal mass loading. Subsequently, the wet film is immersed in the bath of mixture of DIW and ethanol with various volume ratios (DIW: ethanol = 3:1, 4:1 and 5:1 or pure DIW) and time (e.g., 90 minutes for 1.5-mm wet film in non-solvent bath of DIW: ethanol = 3:1 to obtain 40 mg/cm^2 mass loading). The electrodes were then dried at 80 °C overnight before testing.

2.2 Structural and mechanical characterization

The morphology of surface and cross-sectional area of as-prepared LFP electrodes was characterized by scanning electron microscopy (SEM) and energy dispersive spectroscopy (EDS) (FEI Inspect F50). The pore size distribution was measured by mercury intrusion porosimeter (AutoPore IV 9500, Micromeritics Instrument Corporation). The compression test was performed on RSA-G2 Solids Analyzer (TA Instruments). The compression test samples were placed on the platform with both fixtures of the equipment contacting the upper and bottom surfaces, respectively, at the initial status. The strain rate was set up as 0.005 mm/s and force increased to the maximum value (35 N) before cutting off.

2.3 Electrochemical measurements

The prepared free-standing LFP electrodes were cut into disks with diameter of 12.7 mm before coin-cell assembly. CR2032 coin-cells were built by pairing LFP electrode and lithium chip as working and counter electrode, respectively, with one layer of Celgard 2400 polymer separator between two electrodes and soaked in electrolyte of 1 M $LiPF_6$ in ethylene carbonate (EC) and ethyl methyl carbonate (EMC) with the mass ratio of 3:7. The cells were assembled inside an argon-filled glovebox with oxygen and moisture level less than 5 ppm. Cyclic voltammetry was tested with multiple scan rates (0.1, 0.15, 0.2 and 0.25 mV/s) within the voltage window of 2.5 to 4.2 V vs. Li^+/Li (Gamry Reference 3000). Electrochemical impedance spectroscopy (EIS) was measured at the frequency from 1 MHz to 0.1 Hz with AC voltage of 10 mV on an electrochemical working station (Gamry Reference 3000). For the galvanostatic test, the cells were charged and

discharged at rate of C/20 (1 C = 170 mA/g) for 2 cycles as formation, followed by cycling at various C-rates between 2.5 V to 4.0 V (LANDT CT3001A).

3 Results and discussion

The fabrication process of low-tortuosity LFP electrodes through phase-inversion method is illustrated in Fig. 1. After preparing slurry containing LFP, PVDF and acetylene black, the slurry is coated on glass slide, and the coated electrode is immersed in non-solvent coagulation bath which is a mixture of DIW and ethanol at varied ratios. After phase-inversion processing, the slurry coating will separate from the glass substrate and form a free-standing film, which is then taken out of the non-solvent bath and completely dried in vacuum at 80 °C to produce the free-standing electrode. As the wet film is immersed in the non-solvent, the thermodynamic equilibrium breaks and demixing occurs in the slurry film to generate polymer-rich and polymer-lean regions. The polymer-rich region solidifies to form the skeleton or matrix of the electrode, and polymer-lean regions become macro- to nano-voids in the electrode after solvents are removed by drying in vacuum. The introduction of ethanol (high miscibility with NMP) in DIW (low miscibility with NMP) increases the miscibility of solvent and non-solvent, hence facilitates instantaneous demixing and the formation of finger-like channels (Fig. 1). On the other hand, with DIW as non-solvent, more delayed demixing occurs which favors the formation of closed cellular pores in more regions of the electrode compared with the case with mixture of DIW and ethanol (Fig. 1)[48,49]. More discussion on the change of thermodynamics in phase inversion with the introduction of ethanol to the non-solvent can be found in the Supplementary Information.

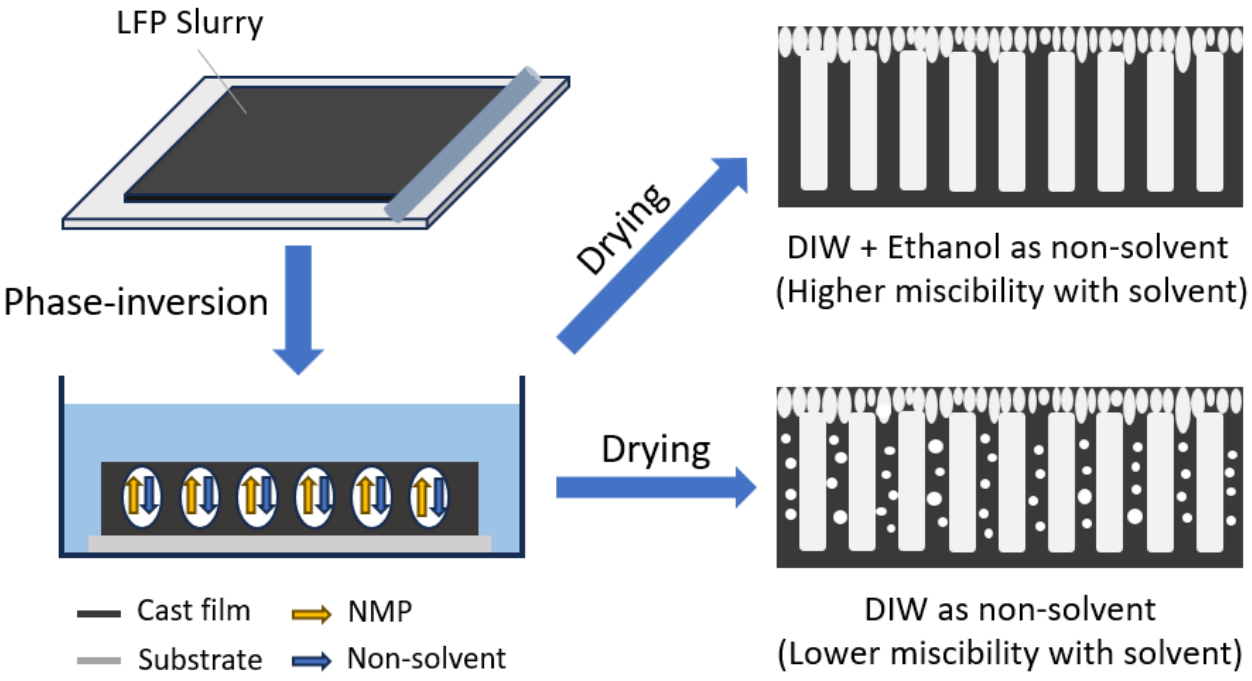

Fig. 1. The schematic process of the fabrication process for free-standing LFP electrode via phase-inversion processes induced by different non-solvents: mixture of DIW and ethanol and pure DIW, and their corresponding electrode structures.

To study the influence of ethanol ratio in the non-solvent, experiments were performed with four ratios of DIW and ethanol (3:1, 4:1, 5:1 and pure DIW) and same immersion time of 90 minutes for the phase-inversion step. The areal mass loading of each electrode was controlled as ~ 40 mg/cm^2 (samples are denoted as WE31-40, WE41-40, WE51-40, and DIW-40). From the scanning electron microscope (SEM) images of four free-standing electrodes shown in Fig. 2 (a-d), the thickness of all four electrodes is around 850 μm. Regarding the structure, finger-like macropores along the thickness direction and a dense skin-layer on top surface can be clearly seen from all four samples, indicating phase inversion occurs. In addition, the element mappings by energy dispersive X-ray spectroscopy (EDS) of four electrodes are illustrated in Fig. S1 to S4, in which uniform element distribution is observed for all four electrodes in polymer-rich region. On the other hand, when DIW to ethanol volume ratio is further reduced to below 3:1, finger-like structures can no longer be observed in the electrodes. For example, when LFP electrodes with mass loading of ~ 40 mg/cm^2 were processed by non-solvent bath with DIW: ethanol ratio = 2:1, 1:1 and 1:2 for 90 minutes, there is not obvious finger-like structure observed according to the SEM images shown in Fig. S5. Based on the existing theory and simulation work on non-solvent induced phase separation[50–54], this phenomenon could be ascribed to the overly strong interaction between the solvent and non-solvent. The EDS of cross-sectional area of WE21-40 electrode (Fig. S6) show a polymer-rich layer with much more fluorine from the PVDF binder on the top surface than in the bulk of the electrode. Since inhomogeneous distribution of binder is detrimental for electrochemical performance and highly undesirable for battery electrodes[55], the investigation of this work about mechanical strength and electrochemical behaviors will focus on the LFP electrodes fabricated by non-solvent bath with ratio of DIW to ethanol no less than 3:1 during phase-inversion process. The rate performance and tortuosity of the WE21-40 electrode, which are inferior to WE31-40 and WE41-40 electrodes, are nonetheless measured and included in Supplementary Information (Fig. S22) for reference.

To investigate the effect of varying DIW-to-ethanol ratio on mechanical properties, compressive stress and strain were measured. The stress vs. strain curve of each sample is plotted in Fig. 2e. To estimate the compressive modulus of each electrode, the linear region is selected to estimate the slope which equals the modulus of the electrode. From Fig. 2f, compressive modulus increases as higher concentration of ethanol was added in the non-solvent mixture. For example, WE31-40 electrode exhibits compressive modulus of 18.1 MPa, the highest among all four samples, compared to 4.1 MPa of the one that was only processed by DIW. Furthermore, as the applied force reaches the maximum of the testing equipment (35 N), WE31-40 electrode shows the smallest strain compared to the other three types of electrodes. Both results indicate that the addition of ethanol during phase-inversion processing contributes to the improvement of mechanical properties of free-standing LFP electrodes. To understand the difference in compressive modulus observed in the four samples, we further investigated the microstructure of the electrode matrix, since the modulus of the electrode is mainly determined by the matrix and the four samples appear to have similar finger-like macropores. As illustrated in high-

magnification SEM image of the matrix regions (Fig. S7), the matrix of the DIW-40 electrode has obvious closed-cell pores, whereas the WE31-40 electrode shows more uniform structure with no obvious large pores. The pore size distribution in WE31-40 and DIW-40 electrodes are also characterized by mercury porosimetry analysis (Fig. S8), in which WE31-40 show more pores of sub-μm size but DIW-40 shows significantly more pores of size around 100 μm. The mercury porosity analysis confirms the observation from the SEM images of the polymer-rich region in Fig. S7. It is noted that some large finger-like pores and cellular pores that are not directly assessable through the surface but rather through a small neck will contribute to pore volume at the size of the small neck in the mercury porosimetry analysis results. Furthermore, the mercury porosimetry instrument used (AutoPore IV 9500, Micrometrics) can only measure pore size up to 360 μm, hence the pore size distribution in Fig. S8 cuts off at this value.

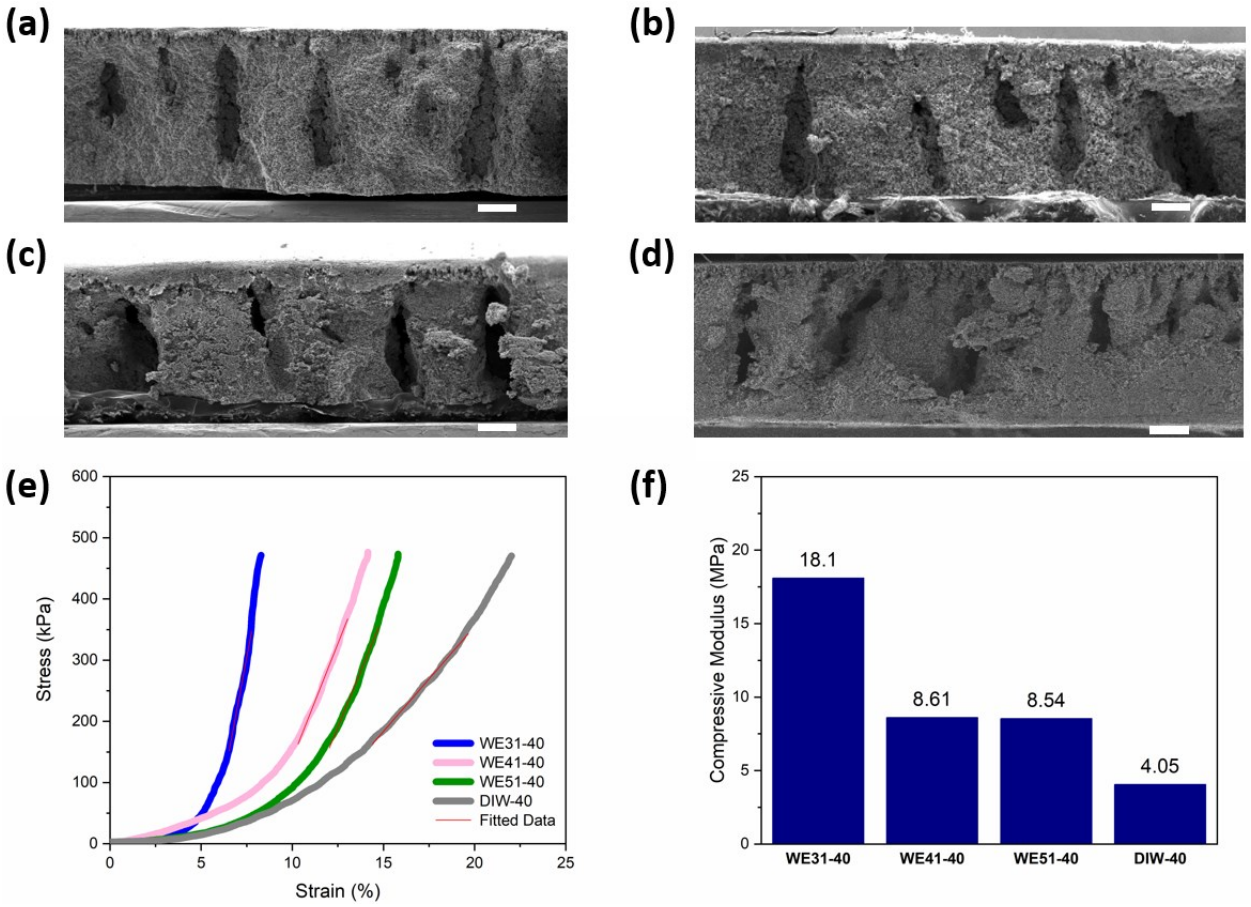

Fig. 2. SEM images of cross-sectional area of (a) WE31-40, (b) WE41-40, (c) WE51-40 and (d) DIW-40 electrodes (scale bar: 200 μm); (e) Stress-strain curves of four electrodes from compression test; (f) Compression modulus of each electrode estimated from the linear part of stress-strain curve.

The rate capability of these four samples at various C-rates is compared in Fig. 3a. The results demonstrate that four electrodes deliver similar specific discharge capacity at low C-rates (< 0.5

C). As C-rate increases, however, WE31-40 electrode retains the highest specific capacity of 152.0, 132.7 and 73.3 mAh/g at 0.5 C, 1 C and 2 C, respectively, compared to the other three electrodes. Moreover, the electrodes produced with higher ethanol ratio in phase-inversion process also demonstrate lower overpotential from the voltage profiles (Fig. 3b, 3c and S9). For the cycling stability (Fig. 3d), with the similar areal mass loading, the electrodes fabricated with mixture bath of ethanol and DIW all reveal advantageous capacity retention of 89.3% (WE31-40), 75.1% (WE41-40) and 71.2% (WE51-40), respectively, after 100 cycles at 0.5 C, compared to 57.3% for DIW-40 electrode. After cycling, the structures inside the electrodes were well maintained according to the SEM images of the cross-sectional areas in four electrodes shown in Fig. S10.

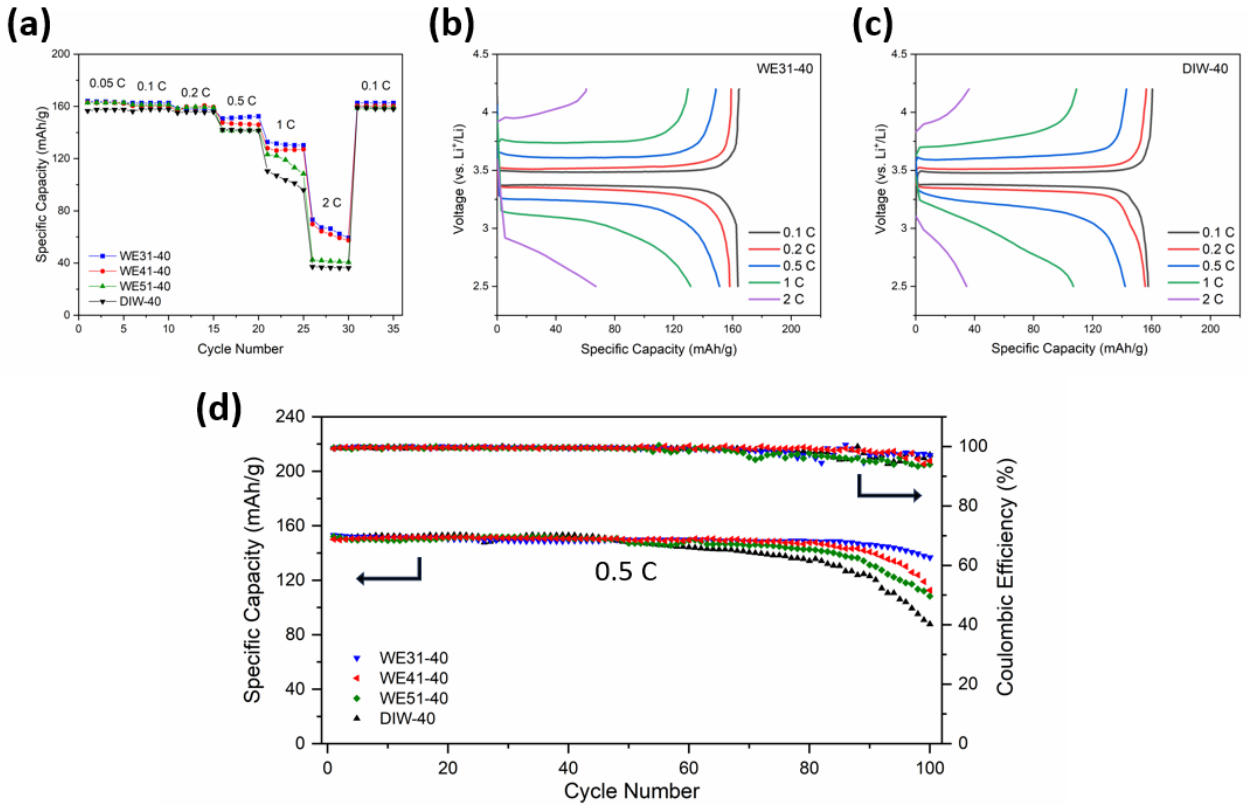

Fig. 3. (a) Rate performance of WE31-40, WE41-40, WE51-40 and DIW-40 electrodes from 0.05 C to 2 C; (b) Voltage profile of WE31-40 electrode during charge and discharge at various C-rates; (c) Voltage profile of DIW-40 electrode during charge and discharge at various C-rates; (d) Discharge capacity and coulombic efficiency of WE31-40, WE41-40, WE51-40 and DIW-40 electrodes at 0.5 C.

To investigate the reasons behind the improved performance of electrodes prepared by the mixture of ethanol and DIW during phase-inversion process, electrochemical impedance spectroscopy (EIS) was applied to measure the resistance of the half-cells and evaluate the kinetics of each free-standing LFP electrode. As shown in the Nyquist plot in Fig. 4a, the internal resistance (R_u) of each curve is located on the first intercept on the Re(Z) axis and charge transfer resistance (R_{ct}) can be estimated by the second intercept on the Re(Z) axis from fitting the semi-circle of each

curve. The equivalent circuit to analyze EIS data is shown in the inset of Fig. 4a. Similar R_u is measured from four half cells containing LFP electrode fabricated by different ratio of ethanol and DIW. However, with a higher ratio of ethanol in phase-inversion process, WE31-40 electrode demonstrates the lowest R_{ct} of 52.9 Ω among these four electrodes, while DIW-40 possessed the highest resistance of 83.6 Ω for charge transfer. In the low-frequency region, according to the semi-infinite linear diffusion and equation (S3), Warburg coefficient (σ) can be obtained by linearly fitting the Warburg impedance (Z_W) versus reverse square root of angular frequency ($\omega^{-1/2}$). Based on the relation between diffusion coefficients of lithium-ion (D_{Li^+}) and Warburg coefficient expressed by equation (S4), D_{Li^+} can be calculated with the low-frequency data of the EIS. For example, WE31-40 electrode reveals the highest D_{Li^+} of 6.70×10^{-9} cm^2/s compared to the other three LFP electrodes (Table S2), demonstrating that lithium-ion diffusion is facilitated in electrodes fabricated with non-solvent bath containing higher ratio of ethanol in phase-inversion process. Additionally, cyclic voltammetry (CV) is implemented to study the kinetics of these four electrodes. From the cyclic voltammograms, which were performed at the scan rate of 0.1 mV/s, illustrated in Fig. 4c, WE31-40 electrode exhibits the highest peak current in both anodic and cathodic region and smallest gap between the peaks, which indicates the lowest overpotential. As ethanol ratio decreases in the non-solvent bath, lower peak current and larger overpotential of as-prepared electrodes are demonstrated (Fig. S11). These results indicate that for the phase-inversion-based electrode fabrication process, lithium-ion diffusion and reaction kinetics are enhanced for the electrodes as the ethanol-to-DIW ratio increases in the non-solvent bath. It is noted that the D_{Li^+} measured from Warburg impedance analysis reflects mostly the through-plan diffusion, which will benefit from the finger-like channels along the thickness direction created by the phase inversion process.

Additionally, galvanostatic intermittent titration technique (GITT) was applied to evaluate the lithium-ion diffusion for the fabricated electrodes. From Fig. 4f, similar static potential was demonstrated by all four electrodes (~ 3.43 V). With a higher ratio of water during phase-inversion process, however, the electrode shows larger overpotential, which indicates larger resistance in the cell (Fig. S13). Lithium-ion diffusion coefficients of each electrode are estimated from the GITT measurement as 4.90×10^{-10}, 4.36×10^{-10}, 2.97×10^{-10}, and 1.30×10^{-10} cm^2/s for WE31-40, WE41-40, WE51-40, and DIW-40, respectively. The trend of D_{Li^+} from GITT measurement is consistent with that from the EIS measurement, further validating the benefits in electrochemical performances brought by using higher ethanol-to-DIW ratio in the non-solvent bath. The detailed procedure of obtaining diffusion coefficients from the data via GITT measurement is provided in Supplementary Information.

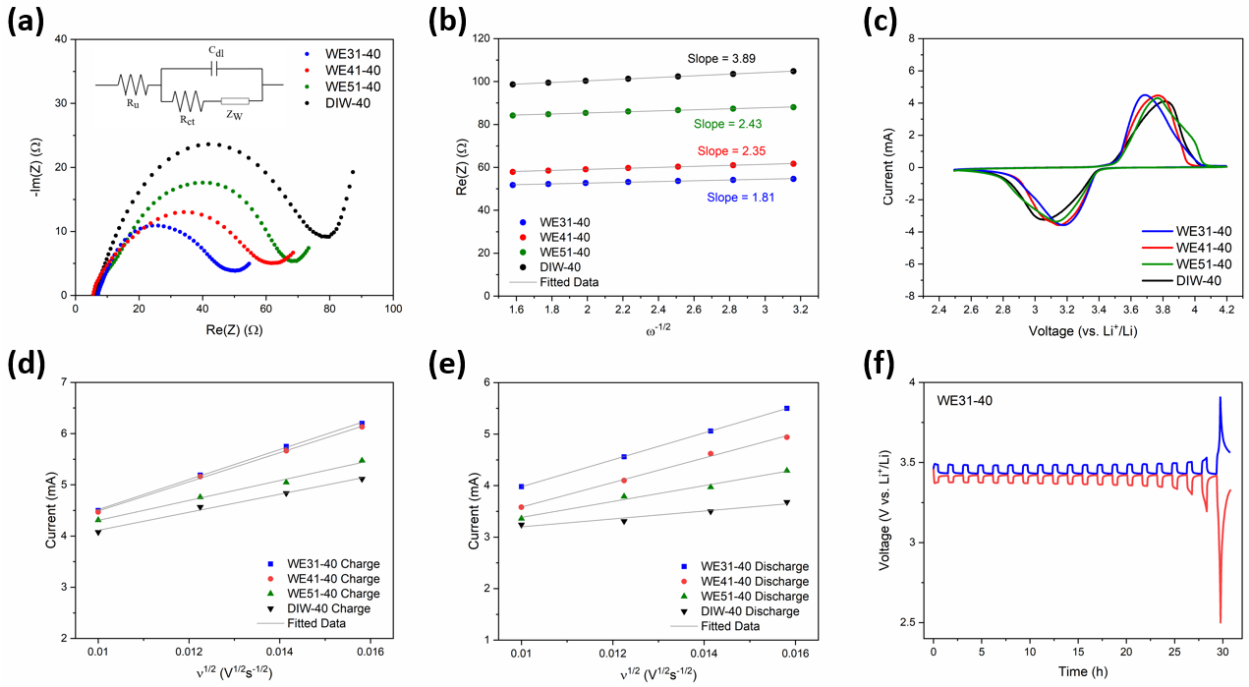

Fig. 4. (a) Nyquist plots of WE31-40, WE41-40, WE51-40 and DIW-40 electrodes; (b) Real impedance of low-frequency region from Nyquist plots and fitted data of impedance vs. inverse square root of angular frequency ($\omega^{-1/2}$); (c) Cyclic voltammograms of WE31-40, WE41-40, WE51-40 and DIW-40 electrodes at scan rate of 0.1 mV/s; Linearly fitted data of peak current vs. square root of scan rate at (d) anodic and (e) cathodic region of cyclic voltammograms. (f) GITT profile of WE31-40 electrode.

Tortuosity in the electrode describes the degree of twisting for lithium-ion diffusion pathways in the electrode. It is one of the key factors that affects the kinetics of the electrode. In this work, tortuosity of as-prepared LFP electrodes was measured via DC-polarization method with symmetric cell model demonstrated in the inset of Fig. 5a. Note that because of the configuration of the symmetric cell, the measured tortuosity reflects mostly through-plan tortuosity. In the symmetric cell, free-standing LFP electrode is sandwiched by two layers of polymer separator and lithium chip on each side. As shown in Fig. 5a, a small current is initially applied to generate a concentration gradient in the cell, followed by relaxing. The same method was applied to measure the intrinsic diffusivity of the electrolyte, where instead of free-standing LFP electrode, PTFE O-ring is used to separate the two layers of polymer separator and lithium chips on each side as shown in Fig. S14. The measured intrinsic diffusivity of the electrolyte is 9.59×10^{-7} cm^2/s, which matches the value in the literature[56,57]. For the measurements of four electrodes fabricated by varied ratios of ethanol to DIW, the tortuosity is 7.85, 9.76, 14.1 and 15.1 for WE31-40, WE41-40, WE51-40, and DIW-40, respectively, as illustrated in Fig. 5b and 5c. These results confirm that higher ratio of ethanol assists to build electrodes with lower tortuosity, which boosts the lithium-ion diffusion, leading to the improvement in kinetics and rate performance. Moreover, the enhanced ion transport contributes to decreasing the overpotential, which improves the cycling stability of the cell.

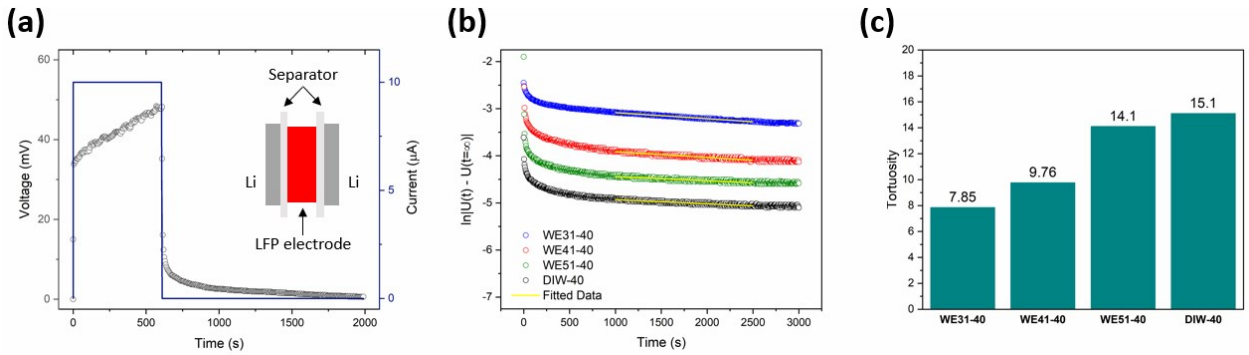

Fig. 5. (a) Voltage change and current applied in DC-polarization (inset: schematic picture of parts in the symmetric cell for tortuosity measurement); (b) Plots of ln|U(t) – U(t = ∞)| versus time of WE31-40, WE41-40, WE51-40 and DIW-40 electrodes and fitted data of linear region in each plot; (c) Estimated tortuosity of each electrode based on the fitted data of DC-polarization.

Besides the composition of non-solvent, we discovered that immersion time is another key factor that affects the structure of the electrodes fabricated by the phase inversion method. For a wet film of the same composition but different thicknesses and hence different areal mass loadings, the immersion time can be adjusted to achieve similar tortuosity in the as-fabricated electrodes. LFP electrodes with areal mass loadings of 20, 30 and 40 mg/cm^2 were prepared using the same non-solvent (DIW: ethanol volumetric ratio of 3:1) and denoted as WE31-20, WE31-30, and WE31-40 respectively. When controlling the immersion time to be 15, 45 and 90 min, respectively, all three electrodes achieve similar finger-like structures (Fig. 2a and Fig. S15). Moreover, the tortuosity of WE31-20, WE31-30, and WE31-40, as measured by the DC-polarization method, are almost the same at 7.44, 7.64 and 7.85, respectively (Fig. 6a). To further study how immersion time affects the tortuosity, using nonsolvent bath with water: ethanol 3:1 v:v ratio, we prepared electrodes of the same mass loading (20 mg/cm^2) but subjected to different immersion time (10 min, 15 min, 30 min, 45 min), denoted as WE31-20-10min to WE31-20-45min. The tortuosity of these samples was measured by DC-polarization tests. Based on the results shown in Fig. S16 and Table S6, for the areal mass loading and immersion time studied, there is an increasing trend for tortuosity as the immersion time increases. These results show the tortuosity of the electrode prepared by the phase inversion process can be modulated by varying the immersion time.

The electrochemical performances of the WE31-20 and WE31-30 samples are also characterized and compared with those of WE31-40. Nyquist plot (Fig. 6b) shows the charge transfer resistances of WE31-20 and WE31-30 are 31.1 and 35.9 Ω respectively, compared to a value of 52.9 Ω for WE31-40. Lithium-ion diffusion coefficient of 1.55×10^{-8} cm^2/s for WE31-20 and of 1.19×10^{-8} cm^2/s for WE31-30 was estimated from the low-frequency region of the electrochemical impedance (Fig. S17), both of which are slightly higher than the diffusion coefficient of 6.70×10^{-9} cm^2/s for WE31-40 measured by the same method. The slightly better Li^+ diffusion in WE31-20 and WE31-30 is mainly ascribed to the lower mass loading. Their narrow advantages on mass transport over WE31-40 electrode are also reflected in the cyclic voltammograms as the two electrodes with less mass loading demonstrate higher peak current and smaller peak distance (Fig. 6c). Furthermore, the GITT data (Fig. S21) indicates smaller overpotential and better lithium-ion

diffusion for WE31-20 (1.50×10^{-9} cm^2/s) and WE31-30 (1.18×10^{-9} cm^2/s) electrode compared to WE31-40 electrode (4.90×10^{-10} cm^2/s). For the rate performance shown in Fig. 6d, three electrodes share a similar rate capability when C-rate is under 1 C, where discharge specific capacities of the three electrodes differ by less than 10 mAh/g at each corresponding rate. As C-rate goes up to 2 C, WE31-20 electrode exhibits an excellent performance of 95.4 mAh/g compared to the other electrodes, which is expected since this electrode has the smallest tortuosity and thickness (areal mass loading) among the three samples. For cycling stability, the lower resistance and improved kinetics assist the electrodes with less mass loading to maintain a more stable capacity retention after 100 cycles of charge and discharge at 0.5 C according to Fig. 6e. In summary, similar tortuosity in the electrodes with varied areal mass loading is successfully achieved with the same non-solvent composition during phase-inversion fabrication by adjusting the immersion time. Largely similar electrochemical performances were demonstrated by the three electrodes with similar tortuosity but different areal mass loading, with the electrode having the smallest loading inevitably showing a small margin of performance advantage.

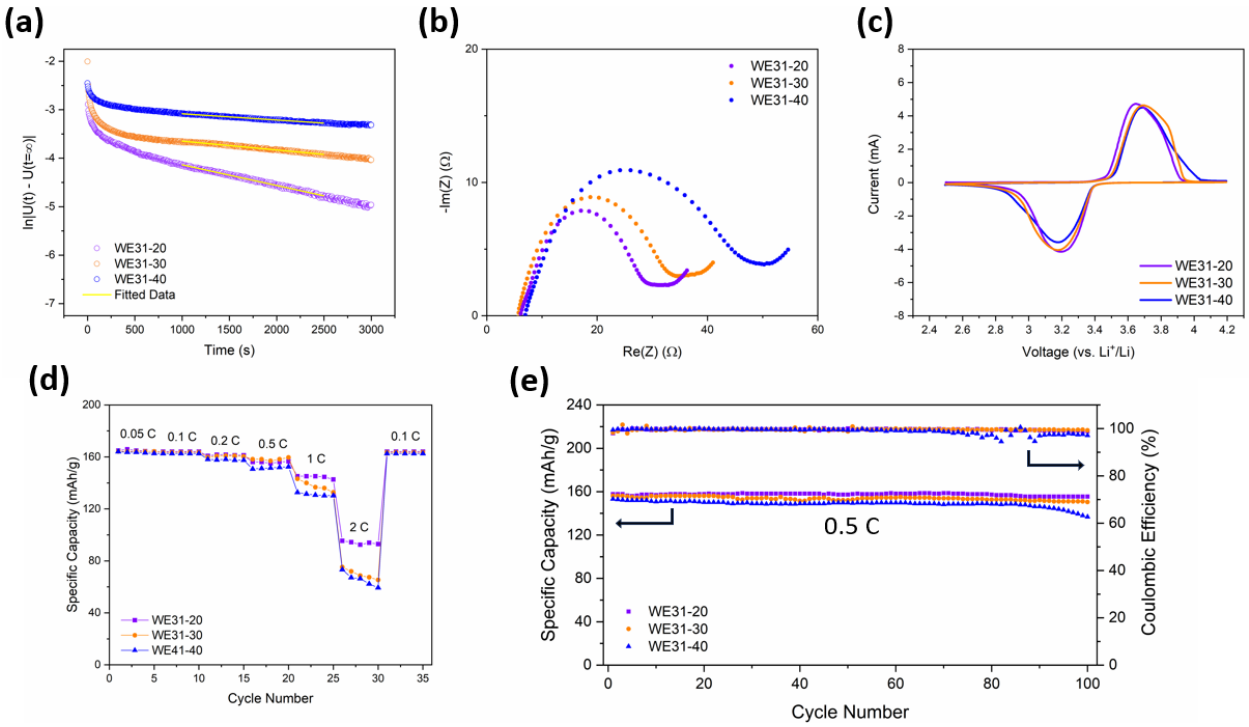

Fig. 6. (a) Plots of $\ln|U(t) - U(t = \infty)|$ versus time of WE31-20, WE31-30 and WE31-40 electrodes and fitted data of linear region in each plot; (b) Nyquist plots of WE31-20, WE31-30 and WE31-40 electrodes; (c) Cyclic voltammograms of WE31-20, WE31-30 and WE31-40 electrodes at scan rate of 0.1 mV/s; (d) Rate performance of WE31-20, WE31-30 and WE31-40 electrodes from 0.05 C to 2 C; (e) Discharge capacity and coulombic efficiency of WE31-20, WE31-30 and WE31-40 electrodes at 0.5 C.

4 Conclusion

In conclusion, we demonstrate an approach to not only construct low-tortuosity structures in electrodes with high areal mass loading to facilitate lithium-ion diffusion for high performance, but also improve the compressive modulus by tuning composition of non-solvent in phase-inversion fabrication. To achieve these two targets, ethanol is mixed with deionized water at various ratios to form the non-solvent bath in the phase-inversion process. As a comparison to the LFP electrode processed by only water, the electrodes processed by mixture of water and ethanol provides a higher compressive modulus. Moreover, the LFP electrode fabricated by non-solvent with ethanol exhibits an advantageous rate performance and cycling stability. Additionally, similar tortuosity was successfully achieved in the free-standing LFP electrodes of various thickness by regulating the immersion time in the same non-solvent. This work advances the phase-inversion based method for fabricating low-tortuosity battery electrode, in that it provides an effective strategy to build low-tortuosity thick electrode for LIBs with high performance along with enhanced mechanical properties and more precise control of the microstructure in the electrode.

Acknowledgements

This material is based upon work supported by the National Science Foundation under Grants No. 1752378 (Y. Zhang and S. Hu) and No. 2323475 (Y. Xiao and L. Chen). Any opinions, findings, and conclusions or recommendations expressed in this material are those of the authors and do not necessarily reflect the views of the National Science Foundation. S. Hu was partially supported by Iowa Economic Development Authority's Iowa Energy Center under Grant No. 20-IEC-016.

Conflict of Interest

The authors have no conflict of interests.

References

1 J. B. Goodenough and K. S. Park, *J. Am. Chem. Soc.*, 2013, **135**, 1167–1176.

2 N. Nitta, F. Wu, J. T. Lee and G. Yushin, *Mater. Today*, 2015, **18**, 252–264.

3 Y. Liu, Y. Zhu and Y. Cui, *Nat. Energy*, 2019, **4**, 540–550.

4 J. Li, J. Fleetwood, W. B. Hawley and W. Kays, *Chem. Rev.*, 2021, **122**, 903–956.

5 J. Chang, Q. Huang, Y. Gao and Z. Zheng, *Adv. Mater.*, 2021, **33**, 2004419.

6 Y. Kuang, C. Chen, D. Kirsch and L. Hu, *Adv. Eng. Mater.*, 2019, **9**, 1901457.

7 Y. Chen, B. Zhao, Y. Yang and A. Cao, *Adv. Eng. Mater.*, 2022, **12**, 2201834.

8 M. Ebner, D. W. Chung, R. E. García and V. Wood, *J. Power Sources*, 2009, **188**, 592–600.

9 I. V. Thorat, D. E. Stephenson, N. A. Zacharias, K. Zaghib, J. N. Harb and D. R. Wheeler, *J. Power Sources*, 2009, **188**, 592–600.

10 H. Zheng, J. Li, X. Song, G. Liu and V. S. Battaglia, *Electrochim. Acta*, 2012, **71**, 258–265.

11 M. J. Lain and E. Kendrick, *J. Power Sources*, 2021, **493**, 229690.

12 Z. Du, D. L. Wood, C. Daniel, S. Kalnaus and J. Li, *J. Appl. Electrochem.*, 2017, **47**, 405–415.

13 X. Zhang, Z. Ju, Y. Zhu, K. J. Takeuchi, E. S. Takeuchi, A. C. Marschilok and G. Yu, *Adv. Eng. Mater.*, 2021, **11**, 2000808.

14 L. Li, R. M. Erb, J. Wang, J. Wang and Y. M. Chiang, *Adv. Eng. Mater.*, 2019, **9**, 1802472.

15 J. S. Sander, R. M. Erb, L. Li, A. Gurijala and Y. M. Chiang, *Nat. Energy*, 2016, **1**, 16099.

16 C. T. C. Wan, R. R. Jacquemond, Y. M. Chiang, K. Nijmeijer, F. R. Brushett and A. Forner-Cuenca, *Adv. Mater.*, 2021, **33**, 2006716.

17 F. Shen, R. A. Jonson, D. Y. Parkinson and M. C. Tucker, *J. Am. Ceram. Soc.*, 2022, **105**, 90–98.

18 M. R. Asghar, Y. Zhang, A. Wu, X. Yan, S. Shen, C. Ke and J. Zhang, *J. Power Sources*, 2018, **379**, 197–205.

19 J. Wang, M. Wang, N. Ren, J. Dong, Y. Li and C. Chen, *Energy Storage Mater.*, 2021, **39**, 287–293.

20 J. Wu, Z. Ju, X. Zhang, K. J. Takeuchi, A. C. Marschilok, E. S. Takeuchi and G. Yu, *Nano Lett.*, 2021, **21**, 9339–9346.

21 J. Wang, M. Wang, J. Si, Y. Zhu and C. Chen, *Chem. Eng. J.*, 2023, **451**, 138651.

22 J. Wu, Z. Ju, X. Zhang, X. Xu, K. J. Takeuchi, A. C. Marschilok, E. S. Takeuchi and G. Yu, *ACS Nano*, 2022, **16**, 4805–4812.

23 J. Wu, Z. Ju, X. Zhang, C. Quilty, K. J. Takeuchi, D. C. Bock, A. C. Marschilok, E. S. Takeuchi and G. Yu, *ACS Nano*, 2021, **15**, 19109–19118.

24 W. Wahyudi, Z. Cao, P. Kumar, M. Li, Y. Wu, M. N. Hedhili, T. D. Anthopoulos, L. Cavallo, L. J. Li and J. Ming, *Adv. Funct. Mater.*, 2018, **28**, 1802244.

25 A. B. Resing, C. Fukuda and J. G. Werner, *Adv. Mater.*, 2023, **35**, 2209694.

26 K. H. Chen, M. J. Namkoong, V. Goel, C. Yang, S. Kazemiabnavi, S. M. Mortuza, E. Kazyak, J. Mazumder, K. Thornton, J. Sakamoto and N. P. Dasgupta, *J. Power Sources*, 2020, **471**, 228475.

27 H. Wang, J. Li, Z. Miao, K. Huang, Y. Liao, X. Xu, J. Meng, Z. Li and Y. Huang, *ACS Appl. Mater. Interfaces*, 2023, **15**, 26824–26833.

28 D. Dang, Y. Wang, S. Gao and Y. T. Cheng, *Carbon*, 2020, **159**, 133–139.

29 B. Delattre, R. Amin, J. Sander, J. De Coninck, A. P. Tomsia and Y.-M. Chiang, *J. Electrochem. Soc.*, 2018, **165**, A388–A395.

30 Y. Hwa, E. Yi, H. Shen, Y. Sung, J. Kou, K. Chen, D. Y. Parkinson, M. M. Doeff and E. J. Cairns, *Nano Lett.*, 2019, **19**, 4731–4737.

31 G. Du, Y. Zhou, X. Tian, G. Wu, Y. Xi and S. Zhao, *Appl. Surf. Sci.*, 2018, **453**, 493–501.

32 Y. Guo, Y. Jiang, Q. Zhang, D. Wan and C. Huang, *J. Power Sources*, 2021, **506**, 230052.

33 S. Yang, C. Zhou, Q. Wang, B. Chen, Y. Zhao, B. Guo, Z. Zhang, X. Gao, R. Chowdhury, H. Wang, C. Lai, N. P. Brandon, B. Wu and X. Liu, *Energy Environ Mater.*, 2022, **5**, 1332–1339.

34 X. Zhang, Z. Hui, S. King, L. Wang, Z. Ju, J. Wu, K. J. Takeuchi, A. C. Marschilok, A. C. West, E. S. Takeuchi and G. Yu, *Nano Lett.*, 2021, **21**, 5896–5904.

35 X. Zhang, Z. Ju, L. M. Housel, L. Wang, Y. Zhu, G. Singh, N. Sadique, K. J. Takeuchi, E. S. Takeuchi, A. C. Marschilok and G. Yu, *Nano Lett.*, 2019, **19**, 8255–8261.

36 C. Huang, M. Dontigny, K. Zaghib and P. S. Grant, *J. Mater. Chem. A*, 2019, **7**, 21421–21431.

37 Y. Zhang, M. Shahriar and S. Hu, *J. Mater. Chem. A*, 2023, **11**, 11849–11858.

38 T. Meng, Z. Geng, F. Ma, Y. Liu, X. Xu and H. Zhang, *Electrochim. Acta*, 2023, **450**, 142268.

39 H. Ren, Y. Wang, D. Cao, W. Gedney, T. Ji, X. Sun and H. Zhu, *Energy Environ Mater.*, 2023, **6**, e12584.

40 Y. Wang, Y. Zhang, D. Cao, T. Ji, H. Ren, G. Wang, Q. Wu and H. Zhu, *Small Methods*, 2023, **7**, 2201344.

41 X. Yang, Y. Chen, M. Wang, H. Zhang, X. Li and H. Zhang, *Adv. Funct. Mater.*, 2016, **26**, 8427–8434.

42 S. Ashtiani, M. Khoshnamvand, P. Číhal, M. Dendisová, A. Randová, D. Bouša, A. Shaliutina-Kolešová, Z. Sofer and K. Friess, *RSC Adv.*, 2020, **10**, 40373–40383.

43 G. R. Guillen, Y. Pan, M. Li and E. M. V. Hoek, *Ind. Eng. Chem. Res.*, 2011, **50**, 3798–3817.

44 Z. Wang, C. Dai, K. Chen, Y. Wang, Q. Liu, Y. Liu, B. Ma, L. Mi and W. Mao, *J. Power Sources*, 2022, **551**, 232176.

45 D. J. Arnot, K. S. Mayilvahanan, Z. Hui, K. J. Takeuchi, A. C. Marschilok, D. C. Bock, L. Wang, A. C. West and E. S. Takeuchi, *Acc. Mater. Res.*, 2022, **3**, 472–483.

46 C. Chen, Y. Zhang, Y. Li, Y. Kuang, J. Song, W. Luo, Y. Wang, Y. Yao, G. Pastel, J. Xie and L. Hu, *Adv. Energy Mater.*, 2017, **7**, 1700595.

47 J. Cannarella and C. B. Arnold, *J. Power Sources*, 2014, **245**, 745–751.

48 A. Bowino, G. Capannelli, S. Munari and A. Turturro, *J. Polym. Sci., Part B*, 1988, **26**, 785–794.

49 W. Lu, Z. Yuan, Y. Zhao, H. Zhang, H. Zhang and X. Li, *Chem. Soc. Rev.*, 2017, **46**, 2199–2236.

50 D. R. Tree, L. F. Dos Santos, C. B. Wilson, T. R. Scott, J. U. Garcia and G. H. Fredrickson, *Soft Matter*, 2019, **15**, 4614–4628.

51 C. E. Udoh, V. Garbin and J. T. Cabral, *Langmuir*, 2016, **32**, 8131–8140.

52 J. G. Wijmans, H. J. J. Rutten and C. A. Smolders, *J. Polym. Sci. Polym. Phys. Ed.*, 1985, **23**, 1941–1955.

53 A. J. Reuvers and C. A. Smolders, *J. Membrane Sci.*, 1987, **34**, 67–86.

54 C. Cohen, G. B. Tanny and S. Prager, *J. Polym. Sci. Polym. Phys. Ed.*, 1979, **17**, 477–489.

55 T. Lombardo, A. C. Ngandjong, A. Belhcen and A. A. Franco, *Energy Storage Mater.*, 2021, **43**, 337–347.

56 M. T. Ong, O. Verners, E. W. Draeger, A. C. T. Van Duin, V. Lordi and J. E. Pask, *J. Phys. Chem. B*, 2015, **119**, 1535–1545.

57 A. Nyman, M. Behm and G. Lindbergh, *Electrochim. Acta*, 2008, **53**, 6356–6365.